JPhys Energy

PAPER • OPEN ACCESS

Electrical barriers and their elimination by tuning (Zn,Mg)O buffer composition in Cu(In,Ga)S_2 solar cells: systematic approach to achieve over 14% power conversion efficiency

To cite this article: Mohit Sood *et al* 2022 *J. Phys. Energy* **4** 045005

Journal of Physics: Energy

PAPER

Electrical barriers and their elimination by tuning (Zn,Mg)O buffer composition in Cu(In,Ga)S_2 solar cells: systematic approach to achieve over 14% power conversion efficiency

Mohit Sood[1,*], **Poorani Gnanasambandan**[1,2], **Damilola Adeleye**[1], **Sudhanshu Shukla**[1], **Noureddine Adjeroud**[2], **Renaud Leturcq**[2] and **Susanne Siebentritt**[1]

[1] Laboratory for Photovoltaics, Department of Physics and Materials Science, University of Luxembourg, Belvaux L-4422, Luxembourg
[2] Material Research and Technology Department, Luxembourg Institute of Science and Technology, Belvaux L-4422, Luxembourg
[*] Author to whom any correspondence should be addressed.

E-mail: mohit.sood@uni.lu

Keywords: quasi-Fermi-level splitting, atomic layer deposition, ZnMgO, barrier, rollover

Supplementary material for this article is available online

OPEN ACCESS

RECEIVED
28 March 2022

REVISED
3 August 2022

ACCEPTED FOR PUBLICATION
9 August 2022

PUBLISHED
28 September 2022

Abstract

Traditional cadmium sulfide (CdS) buffer layer in selenium-free Cu(In,Ga)S_2 solar cells leads to reduced open-circuit voltage because of a negative conduction band offset at the Cu(In,Ga)S_2/CdS interface. Reducing this loss necessitates the substitution of CdS by an alternative buffer layer. However, the substitute buffer layer may introduce electrical barriers in the device due to unfavorable band alignment at the other interfaces, such as between buffer/ZnO i-layer. This study aims to reduce interface recombinations and eliminate electrical barriers in Cu(In,Ga)S_2 solar cells using a combination of $Zn_{1-x}Mg_xO$ and Al-doped $Zn_{1-x}Mg_xO$ buffer and i-layer combination deposited using atomic layer deposition and magnetron sputtering, respectively. The devices prepared with these layers are characterized by current–voltage and photoluminescence measurements. Numerical simulations are performed to comprehend the influence of electrical barriers on the device characteristics. An optimal composition of $Zn_{1-x}Mg_xO$ ($x = 0.27$) is identified for a suitable conduction band alignment with Cu(In,Ga)S_2 with a bandgap of ∼1.6 eV, suppressing interface recombination and avoiding barriers. Optimized buffer composition together with a suitable i-layer led to a device with 14% efficiency and an open-circuit voltage of 943 mV. A comparison of optoelectronic measurements for devices prepared with zinc oxide (ZnO) and Al:(Zn,Mg)O shows the necessity to replace the ZnO i-layer with Al:(Zn,Mg)O i-layer for a high-efficiency device.

1. Introduction

Buffer and window layers are essential for *p–n* junction formation and charge carrier separation in heterojunction chalcopyrite solar cells. Traditionally, cadmium sulfide (CdS) buffer layer in combination with intrinsic zinc oxide (ZnO) and aluminum-doped zinc oxide (Al:ZnO) window layer is used as optimum partner for high-efficiency copper indium gallium sulfoselenide (Cu(In,Ga)$(S,Se)_2$) devices [1–6]. One of the reasons for this combination is that these layers have a rather low conduction band offset (CBO) [7, 8], and consequently, there are no electrical barriers at the interfaces in between these layers. Cu(In,Ga)S_2 (CIGSu), the wide bandgap selenium-free counterpart of CIGSe absorber material, has immense potential to be deployed as a top cell in tandem devices together with a Si or CIGSe bottom cell, owing to its tunable direct bandgap (E_G) between 1.54 eV ($CuInS_2$) and 2.53 eV ($CuGaS_2$) [9]. However, the Cu-deficient CIGSu devices fabricated with the traditional CdS buffer layer suffer from dominant interface recombination due to negative or a 'cliff' CBO at the CIGSu/CdS interface [10], which is not present in case of standard low bandgap CIGSe [11]. The presence of this 'cliff'-type CBO at the CIGSu/CdS interface leads to a disparity between the maximum achievable open-circuit voltage given by the quasi-Fermi-level (qFL) splitting and the

actual open-circuit voltage in the device (V_{OC}) [12]. Higher power conversion efficiency (PCE) aspirations thus require the substitution of the CdS buffer layer with alternative buffer layers that possess a higher conduction band minimum (CBM) energy value than CdS. The zinc magnesium oxide ((Zn,Mg)O) and zinc oxy-sulfide (Zn(O,S)) buffers are particularly interesting, as it is possible to modify the bandgap and the CBM energy of the films by tuning the Mg content and O/S ratio in the films, respectively [13–16]. As a matter of fact, the record PCE of 15.5% has been achieved by replacing the CdS/i-ZnO buffer i-layer stack with a bilayer (Zn,Mg)O buffer stack [17]. While there have been numerous studies that explicitly study (Zn,Mg)O as a buffer layer partner for Cu(In,Ga)Se_2 [18–21], detailed study on (Zn,Mg)O as a buffer layer partner for CIGSu is still missing. Here, we investigate (Zn,Mg)O/Al:(Zn,Mg)O as a replacement to CdS/ZnO buffer and i-layer stack using qFLs and V_{OC} measurements to better understand the losses, together with a model of how replacing these layers improves the device performance.

We recently demonstrated a CIGSu device ($E_G \sim 1.57$ eV) with a PCE of 15.2% obtained by successfully substituting the CdS buffer layer with Zn(O,S) buffer layer deposited using chemical bath deposition [12]. By replacing CdS with Zn(O,S), the interface recombination in the device and the difference between qFLs and V_{OC} reduced due to better buffer CBM alignment with CIGSu [12]. We also found that the substitution of CdS with Zn(O,S) buffer layer having higher CBM results in an electrical transport barrier when using ZnO as i-layer in the device. The barrier is apparent as a rollover in the positive power quadrant in the device, which results in low fill factor (FF) and PCE. The CBO between CdS and ZnO has been found to be -0.30 ± 0.10 eV [8]; therefore, the rollover might be caused by a high negative CBO at the Zn(O,S)/ZnO (buffer/i-layer) interface. To achieve high FF in the Zn(O,S) buffer device, Al:(Zn,Mg)O i-layer was used, which led to PCE above 15% [12]. However, the device fabrication process required an additional annealing step (∼200 °C for 10 min) after buffer deposition. This step leads to a reduction in qFLs of the absorber (see figure S1 in the supplementary information), therefore limiting the maximum achievable V_{OC} and PCE of the device.

In this contribution, the replacement of the CdS/i-ZnO (buffer/i-layer) stack is explored by a (Zn,Mg)O/Al:(Zn,Mg)O stack using atomic layer deposition (ALD) and magnetron sputtering process that does not require an additional high-temperature annealing step. The impact of varying Mg composition in the (Zn,Mg)O buffer on CIGSu device properties is explored. Calibrated photoluminescence (PL) measurements are performed on the absorber to extract the qFL values. Current–voltage and external quantum efficiency (EQE) measurements are performed on the completed device to extract the electrical characteristics. The deficit between measured qFLs/e and V_{OC} is investigated and compared for different Mg concentrations in (Zn,Mg)O films. Numerical simulations are performed to comprehend the influence of electrical barriers on device current density–voltage (J–V) characteristics of the fabricated devices. The results presented here show the necessity of properly tuning the CBO at various interfaces in the device to realize high PCE CIGSu devices.

2. CIGSu device fabrication

2.1. Absorber deposition

Cu-poor CIGSu absorbers were prepared on molybdenum (Mo) coated soda-lime glass substrates via a three-stage co-evaporation process at a temperature of ∼570 °C with the final film thickness of ∼2 μm. The detailed procedure is reported in [12]. The desired absorber stoichiometry was obtained by controlling the evaporation flux of the Cu, In, and Ga sources and the duration of the three stages of the process. The final bulk composition of as-grown absorbers was determined using energy-dispersive x-ray spectroscopy (EDS).

2.2. Buffer deposition

$Zn_{1-x}Mg_xO$ buffer layers with three different compositions with $x = 0.27$, 0.30, and 0.37 were deposited in this study. Prior to buffer deposition, all the absorbers were etched in 5% KCN solution for 30 s to remove any oxides, followed by rinsing and storing in deionized water. This was done to prevent possible degradation of optoelectronic properties of chalcopyrite absorbers by air exposure, as observed previously [22, 23]. The samples were blow-dried with nitrogen gas to remove the water layer immediately before introducing them into the ALD reactor. The ALD of the (Zn,Mg)O buffer was carried out in an ALD reactor using diethylzinc (DEZ) and bis(cyclopentadienyl) magnesium ($Mg(Cpt)_2$) as precursors for ZnO and MgO, respectively, with water as co-reactant. $Mg(Cpt)_2$ was heated at 78 ± 3 °C to achieve high-enough vapor pressure. The deposition of $Zn_{1-x}Mg_xO$ ($x = 0.30$) film was carried out at a temperature of 130 °C, and for $Zn_{1-x}Mg_xO$ ($x = 0.27$ and 0.37) the deposition was done at a temperature of 150 °C. A supercycle approach was used to deposit (Zn,Mg)O. One supercycle involves alternating ZnO cycles (DEZ/H_2O) and MgO cycles ($Mg(Cpt)_2/H_2O$) with a ratio chosen to attain the expected composition, and these supercycles were repeated to achieve a thickness of 30 nm.

2.3. i-Layer and transparent conductive oxide window layer deposition

Both ALD and magnetron sputtering were used for i-layer deposition. The sputtering process for Al:(Zn,Mg)O is based on previous work on (Zn,Mg)O [24]. The 2 inch targets of MgO with 2 wt % Al_2O_3 and of (undoped) ZnO were co-sputtered at a power of 80 and 110 W, respectively. Throughout the deposition, 1.0 mTorr partial pressure of argon (99.99%) was maintained with the help of a mass flow controller. Desired composition of Al:$Zn_{1-x}Mg_xO$ ($x = 0.25$) was achieved by tuning the Al:MgO target power.

The composition of deposited films was determined by EDS performed on films grown on Si substrate for ALD-deposited (Zn,Mg)O and on molybdenum-coated soda-lime glass for sputtered Al:(Zn,Mg)O.

After i-layer deposition, a transparent conductive oxide (TCO) window layer (Al:ZnO) was sputtered onto the samples. For this, a 2 wt % Al-doped ZnO single target was sputtered at 140 W. Other growth conditions were the same as for Al:(Zn,Mg)O deposition. The Ni–Al grids were deposited on the samples using e-beam evaporation to complete the device fabrication process. On each sample, several devices of area $\sim$0.5 cm^2 were realized by mechanical scribing.

2.4. Characterization methods

EDS with an operating voltage of 20 kV was used to determine the stoichiometry of as-grown absorbers and buffer layers. For determining the thickness of the ALD-deposited (Zn,Mg)O buffer layer, a Si wafer was placed alongside the CIGSu samples in each run. The thickness of (Zn,Mg)O film on Si wafer was then determined by ellipsometry using an effective medium approximation model. PL measurements were carried out in a home-built system using a steady-state excitation via a continous wave (CW) diode laser of 405 nm wavelength as the excitation source. The raw PL data were acquired through two off-axis mirrors then spectrally resolved and detected by a monochromator and Si charge-coupled device (CCD), respectively. Spectral and intensity corrections are subsequently applied to the raw PL data. The spectral correction is performed with a commercial calibrated halogen lamp. The intensity correction entails the measurement of the laser beam diameter with a CCD camera and the laser power by a photodetector. Photon flux from the laser is calculated and adapted to the air mass (AM) 1.5 solar spectrum photon flux above the bandgap. Thus, an illumination corresponding to '1 sun' for a bandgap of $\sim$1.6 eV is used on the samples. The corrected spectrum is transformed into the energy domain and assessed using Planck's generalized law [25], which describes the dependence of the luminescence yield as a function of absorptivity, temperature, and qFLs. The qFLs are extracted from a fit of the high-energy wing of the PL spectrum, where absorptivity is assumed unity and the temperature is fixed to 300 K [23]. A variation in the qFL value across the absorbers grown in the same run and even on the same absorber was observed (figure S2). We attribute this difference in qFL values to the inhomogeneous heating of the sample stage during absorber deposition.

For measuring device *J–V* properties, a xenon short-arc lamp AAA standard solar simulator was used together with an *IV* source-measure unit. The simulator was calibrated to air mass 1.5 global using a Si reference cell. For determining the EQE of devices, EQE setup consisting of halogen and xenon lamps, a grating monochromator, a chopper, and calibrated reference diodes was used. The current was measured using a lock-in amplifier and the intensity of the light by calibrated reference diodes. Low-temperature *J–V* measurements were performed by mounting the samples in a closed-cycle cryostat chamber, where a base pressure below 4×10^{-3} mbar is maintained. For measuring the *J–V* at one-sun illumination conditions, a cold mirror halogen lamp with an equivalent intensity of 100 mW cm^{-2} was used. The lamp intensity was adjusted by setting the short-circuit current density (J_{sc}) of the sample equal to the value measured under the solar simulator, which was achieved by changing the height of the lamp from the sample. For precise measurement of the sample temperature, a Si-diode sensor glued onto an identical glass substrate was placed just beside the solar cell.

2.5. Numerical simulation

Numerical simulations were done using the solar cell capacitance simulator (SCAPS-1D), which solves the 1D Poisson and continuity equation for electrons and holes, using appropriate boundary conditions at the interfaces and the contacts. The software is developed at the Department of Electronics and Information Systems of the University of Ghent, Ghent, Belgium, under Burgelman *et al* [26]. The device parameters used in this study are reported in table S1.

3. Effect of Mg content in the buffer on device properties

We start by exploring the effect of different compositions of $Zn_{1-x}Mg_xO$ buffer layers on the CIGSu device performance. For this purpose, we used ALD-deposited $Zn_{1-x}Mg_xO$ films with $x = 0.27$, 0.30, and 0.37, with a measured bandgap of 3.8, 3.9, and 4.6 eV, respectively. The composition was chosen based on the following

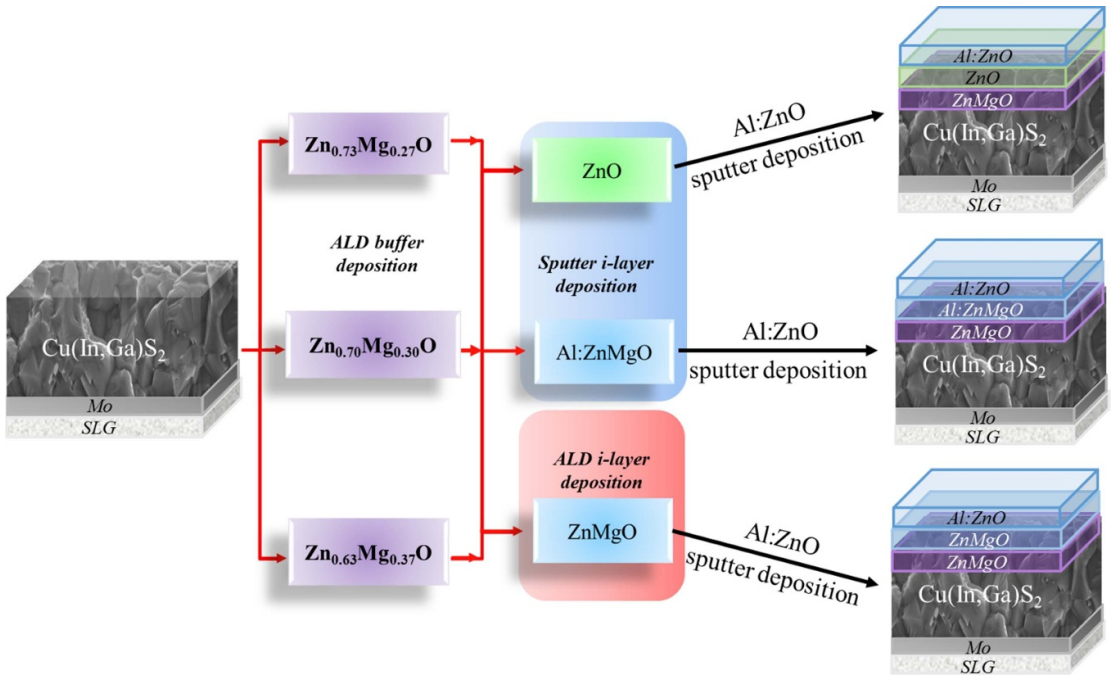

Figure 1. Experimental schematic showing the device fabrication process. The CIGSu absorbers are first processed with $Zn_{1-x}Mg_xO$ buffer layer with $x = 0.27$, 0.30, and 0.37, followed by deposition of either ZnO or Al:(Zn,Mg)O or (Zn,Mg)O i-layer and finally the deposition of Al:ZnO TCO layer.

argument: the CIGSu/CdS device has an activation energy value ∼0.2 eV less than the bulk bandgap of CIGSu for the dominant recombination pathway [12], which implies that the CdS buffer layer has a CBM that is 0.2 eV lower than the CBM of CIGSu [27]. Next, ZnO is known to have a CBO of -0.30 ± 0.10 eV with CdS [8]. Thus, indirectly we can assume CIGSu has a −0.50 eV CBO with ZnO. Now, assuming the increase in bandgap due to Mg incorporation results solely in the increase in CBM of the $Zn_{1-x}Mg_xO$ films, the above composition should yield CIGSu/(Zn,Mg)O devices with CBO of 0.0, 0.1, and 0.8 eV.

The experimental device preparation plan starting from the absorber until TCO deposition is presented in figure 1. The experiments were performed on as-grown CIGSu samples having bulk bandgap ∼1.6 eV with a [Cu]/[In + Ga] (CGI) ∼0.93 and [Ga]/[Ga + In] (GGI) ∼0.12. The deficit between qFLs/e (e being the electron charge) and V_{OC} has been established as interface V_{OC} deficit [28] and is used as the benchmark for making a comparison among different samples. For this, the qFL is measured at different spots for all the absorbers prior to buffer deposition.

Figure 2(a) shows *J*–*V* characteristics of the devices prepared with the three different $Zn_{1-x}Mg_xO$ buffer layers, with either ZnO or Al:(Zn,Mg)O as the i-layer deposited by sputtering. The device *J*–*V* characteristic parameters are reported in table 1, along with locally measured qFL values on the sample before buffer deposition. The device with $Zn_{1-x}Mg_xO$ ($x = 0.27$) buffer layer and sputtered Al:(Zn,Mg)O i-layer exhibits the highest PCE ∼12% among all devices. Independent of the i-layer used, a deterioration in the device PCE is observed with increasing Mg content in the $Zn_{1-x}Mg_xO$ buffer. Between the two i-layers, lower PCE values are displayed by the devices prepared with ZnO i-layer compared to Al:(Zn,Mg)O i-layer devices with the same buffer composition.

Figure 2(b) shows the variation of PCE, FF, and the interface V_{OC} deficit of the devices as a function of the Mg content for devices prepared with both ZnO and Al:(Zn,Mg)O i-layer. The drop in PCE with increasing Mg content in buffer layers can be majorly attributed to a loss of FF (figure 2(b)). In the case of ZnO i-layer devices, the loss in FF is even higher than the Al:(Zn,Mg)O i-layer devices; therefore, the PCE is lower. The loss in FF is due to distortion in the *J*–*V* curve of the devices in the form of 'S shape' in the negative power quadrant and rollover in the positive power quadrant, as evident in the *J*–*V* curve of devices (figure 2(a)).

With the increasing Mg content in the buffer, the interface V_{OC} deficit increases, particularly in the devices prepared with the ZnO i-layer. This indicates an increased qFL loss in the device. The loss originates partially from the absorber degradation after buffer deposition, as the qFL measurements display a drop in qFLs after (Zn,Mg)O buffer deposition (see figure S4, performed on a different sample). Further loss in V_{OC} relative to qFLs measured after buffer deposition might originate from the gradient in electron qFL either in

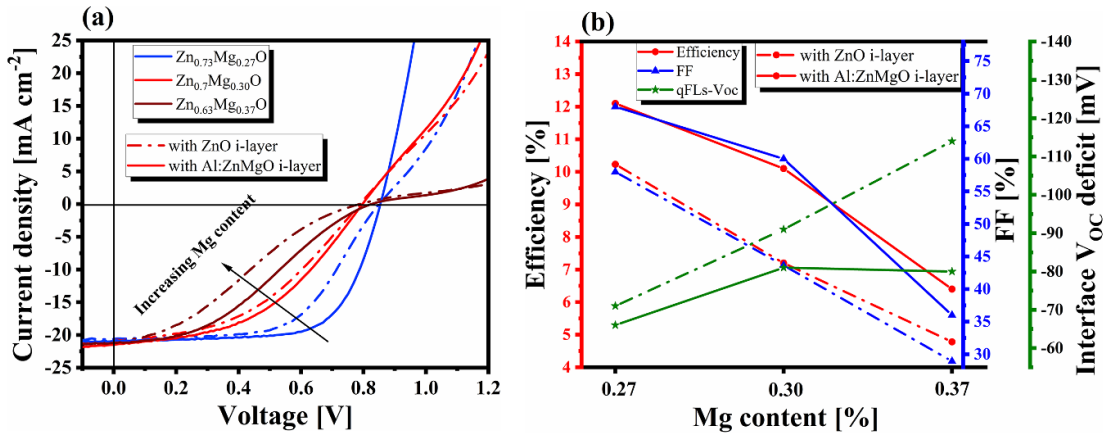

Figure 2. (a) Measured *J*–*V* characteristics of devices with different Mg content in (Zn,Mg)O buffer layers. (b) Scatter chart of device PCE (left axis), FF (right axis), and interface V_{OC} deficit (second right axis) vs. different Mg contents in (Zn,Mg)O buffer layers. The solid lines represent the device with an i-Al:(Zn,Mg)O + Al:ZnO layer, and the dashed–dotted lines represent the device with i-ZnO + Al:ZnO layer on top of the buffer.

Table 1. *J*–*V* characteristics of best CIGSu devices made of $Zn_{1-x}Mg_xO$ buffer with $x = 0.27$, 0.30, and 0.37 and with a sputter-deposited i-ZnO layer or Al:(Zn,Mg)O i-layer and Al:ZnO TCO layer. The qLF values reported are for absorbers before buffer deposition.

$Zn_{1-x}Mg_xO$	PCE (%)	FF (%)	J_{sc} (mA cm^{-2})	V_{OC} (mV)	qFLs at 1 sun (meV)	V_{OC} − qFLs/e (mV)
$x = 0.27$ Al:ZnMgO i-layer	12.1	68	20.9	854	920	−68
$x = 0.27$ ZnO i-layer	10.1	58	20.6	850	921	−71
$x = 0.3$ Al:ZnMgO i-layer	10.1	60	21.2	796	877	−81
$x = 0.3$ ZnO i-layer	7.2	44	20.9	785	876	−91
$x = 0.37$ Al:ZnMgO i-layer	6.4	36	21.5	825	905	−80
$x = 0.37$ ZnO i-layer	4.8	29	21.0	787	901	−114

the vicinity of the absorber surface [28] or within the contact layer. Similar losses have been observed in selenide solar cells with non-optimized contact layers [23]. The presence of negative CBO at the CIGSu/(Zn,Mg)O interface could be one possible origin of this loss. However, the temperature-dependent V_{OC} measurements on the device with the lowest CBM in the $Zn_{1-x}Mg_xO$ buffer (i.e. the one with $x = 0.27$) yield activation energy of the dominant recombination path equal to the bulk bandgap (see figure S3). This excludes the presence of a negative CBO CIGSu/(Zn,Mg)O interface; otherwise, the activation energy would have been less than the bulk bandgap [27, 29]. We show later by simulations that the CBOs at the buffer/i-layer interface are critical parameters for the V_{OC} loss.

The results suggest that the $Zn_{1-x}Mg_xO$ ($x = 0.27$) buffer layer with sputtered Al:(Zn,Mg)O i-layer is the best combination for high device PCE. With the optimized buffer conditions, another CIGSu device with ALD-deposited $Zn_{1-x}Mg_xO$ ($x = 0.27$) buffer layer and sputtered Al:(Zn,Mg)O i-layer was fabricated and equipped with an anti-reflective coating (ARC). The absorber used for this device possessed a qFL of 986 meV with an E_G ~1.63 eV obtained by $\frac{d(EQE)}{dE}$ analysis (see figure S5). The higher E_G is due to slightly higher Ga concentration in the absorber, [Ga]/[Ga + In] ~ 0.18, compared to earlier devices. The *J*–*V* characteristic of the device is presented in figure 3. The device exhibits a PCE of 14.0% with a V_{OC} of 943 mV after light soaking (LS) of 30 min under open-circuit conditions. The V_{OC} obtained is the highest among all the devices fabricated in this study, although even this device possesses a moderate interface V_{OC} deficit of ~40 mV. The higher PCE is a consequence of the improved optoelectronic quality of the absorber and interface quality of the device. The device has a 30 mV lower qFLs/e loss w.r.t. to Shockley–Queisser V_{OC} [30] and 28 mV lower interface V_{OC} deficit compared to the best devices discussed previously. The results thus show that a combination of $Zn_{1-x}Mg_xO$ ($x = 0.27$) buffer layer and sputtered Al:(Zn,Mg)O is ideal for CIGSu devices with a bandgap around 1.6 eV. Achieving even higher PCE needs further improvement in the optoelectronic properties of the absorber.

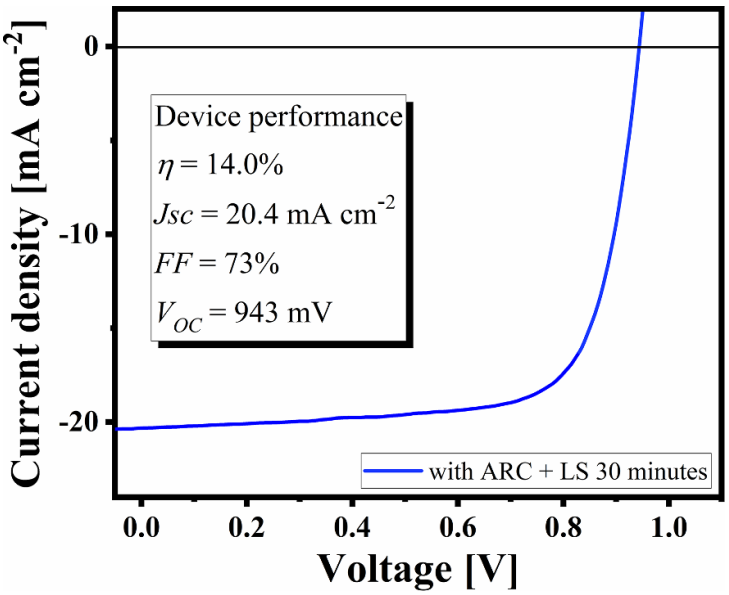

Figure 3. *J–V* curve of the best device prepared with $Zn_{1-x}Mg_xO$ ($x = 0.27$) buffer layer together with Al:(Zn,Mg)O i-layer and Al:ZnO TCO layer. The curve is obtained for a device with an ARC of MgF_2 and light-soaked for 30 min under open-circuit conditions.

4. Numerical simulations for electrical barriers

The *J–V* curves of the devices with $x \geqslant 0.3$ in the $Zn_{1-x}Mg_xO$ buffer layer exhibit 'S shape' in the negative power quadrant and a rollover at a forward bias above their V_{OC} (figure 2). This is a typical sign of an extraction and injection barrier at the front or back contact for charge carriers [31, 32]. The back contact barrier can be excluded, as the device with $Zn_{1-x}Mg_xO$ ($x = 0.27$) buffer layer does not display distortion in the *J–V* curve. Therefore, the front contact barrier is the only viable cause for the 'S shape' and rollover in these devices [32]. This, of course, assumes that ALD buffer deposition does not change absorber properties near the back contact nor the properties of the back contact itself. Using numerical simulations, the effect of a front barrier on the device *J–V* characteristics will be explored here.

The electrical barrier in the devices studied here likely originates from the increased CBM of the (Zn,Mg)O buffer films with increased Mg content, as observed earlier by Minemoto *et al* [13]. The increased CBM also increases the CBO at the absorber/buffer and the buffer/i-layer interface, thus leading to an electrical barrier for photogenerated electrons and the injected electrons. Figure 4(a) shows a simulated conduction band profile of the junction, depicting the two barriers: one for the photogenerated carriers φ_b^{ph} and the other for the injected electrons φ_b^{in}. φ_b^{ph} is the energetic distance between the electron Fermi level at the absorber/buffer interface and the CBM of the buffer at the absorber/buffer interface, and φ_b^{in} is the energetic distance between the electron Fermi level at the i-layer/TCO interface and the CBM of the buffer at the absorber/buffer interface [27]. The ΔE_{Fn} is the drop in Fermi level at the interface, which is required to derive the diode current across the junction.

From figure 4(a), it is clear that the height of the two barriers is equal at equilibrium and is dependent on the position of electron Fermi level at the absorber/buffer interface and position of electron Fermi level at the i-layer/TCO interface, for φ_b^{ph} and φ_b^{in}, respectively. While it is evident that the two barriers are dependent on the CBM of the buffer, the φ_b^{in} is also impacted by the CBM of i-layer. This is because it changes the band bending in the absorber and therefore the position of electron Fermi level at the i-layer/TCO interface. For example, figure 4(b) depicts simulated band diagrams of two devices:

(a) Device with a CBO of 0.2 eV at the absorber/buffer interface, −0.4 eV at the buffer/i-layer interface, and no CBO at the i-layer/TCO interface (the dashed–dotted line in figure 4(b)).
(b) Device with a CBO of 0.2 eV at the absorber/buffer interface, and −0.2 eV at both buffer/i-layer and i-layer/TCO interfaces (the solid line in figure 4(b)).

The CBM of the i-layer in the second device is 0.2 eV higher than the first device (based on observed 0.2 eV increase in the bandgap for Al:(Zn,Mg)O compared to ZnO; see figure S6). Here, we have tried simulating a situation comparable to the case where ZnO or Al:(Zn,Mg)O assumed is used as i-layer in the

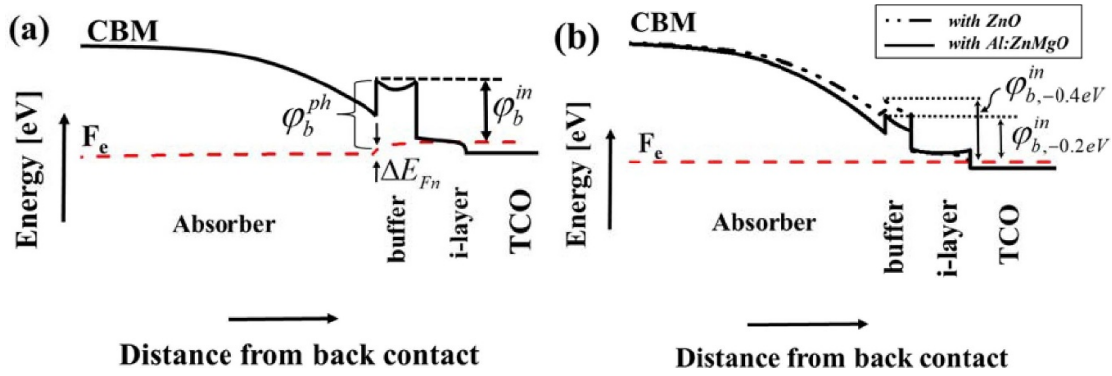

Figure 4. (a) Simulated band diagram of a device showing the injection φ_b^{in} and extraction barrier φ_b^{ph} in a device at forward bias. (b) Simulated equilibrium energy band diagram of devices, one with the Al:(Zn,Mg)O i-layer (solid) and one with the ZnO i-layer (dashed–dotted lines). For simulating the Al:(Zn,Mg)O i-layer device, a CBO of −0.2 eV is introduced at both buffer/i-layer interface and i-layer/TCO interface, whereas for simulating the ZnO i-layer device a CBO of −0.4 eV is introduced at the buffer/ZnO i-layer interface, and a flat conduction band at i-layer/TCO interface.

device. Even though CBO at the absorber/buffer interface and CBO between buffer and the TCO layer are the same, the barrier height in equilibrium φ_b^{in} is different in each case for the two devices. This is because the band bending in the absorber depends on the buffer-i-layer CBO. For device 1 it is 0.510 eV, whereas for device 2 it is 0.678 eV. This shows that the CBM of the i-layer also has an influence on the barrier height in the device.

By varying Mg concentration in buffer and i-layer, we vary either the CBM of the buffer or the CBM of the i-layer in the devices prepared in this study. An increase in φ_b^{ph} and φ_b^{in} is expected with the increase in Mg concentration in the $Zn_{1-x}Mg_xO$ buffer layer and a decrease with an increase in the i-layer, as it is known to increase the CBM of the films [13]. A qualitative method to differentiate and comprehend the impact of different Mg contents in buffer and i-layer on the electrical barriers and the device *J–V* characteristics is to simulate the device in the SCAPS 1D simulator [26, 33]. In the following, the effect of these two barriers is explored with the help of the SCAPS 1D simulator, first separately and then together on device *J–V* characteristics.

We discuss three scenarios: (i) varying CBO at the absorber/buffer interface with constant CBO at the buffer/i-layer; (ii) varying CBO at the buffer/i-layer interface with constant CBO at the absorber/buffer interface; and finally, (iii) varying the CBM in the buffer, thus varying CBO at the absorber/buffer and the buffer/i-layer interface. The first two cases particularly help to distinguish the effect of the CBO at the absorber/buffer interface and the buffer/i-layer interface on the *J–V* curves of the device separately. The parameters used for these simulations are reported in table S1.

We start by looking at the impact of scenario (i) on device *J–V* curves. While there is no experimental equivalent of this situation in this study, it helps us differentiate the effect of CBO at the absorber/buffer from the CBO at the buffer/i-layer (TCO layer) interface. For this, a CIGSu device is simulated in SCAPS-1D, and the buffer CBM energy is varied via changing its electron affinity. A CBO of −0.2 eV at the buffer/i-layer interface and a flat CBO at the i-layer/TCO interface were maintained by changing the CBM of i-layer and TCO equal to the change in buffer CBM energy. This was done to exclude the effects of change in CBO at the buffer/i-layer interface and i-layer TCO on the *J–V* curves of the device. The CBO at the CIGSu/buffer interface was varied from 0.25 to 0.50 eV.

The equilibrium band diagram and the *J–V* characteristics are simulated and presented in figure 5. Itcan be observed that the CBO value $\leqslant$0.35 eV at the CIGSu/buffer interface does not impact the *J–V* curves significantly. However, a CBO value above 0.35 eV results in an 'S shape' in the negative power quadrant, reducing the FF of the device. A CBO $\geqslant$0.50 eV starts affecting the J_{SC} and V_{OC} as well. The 'S shape' originates from a high φ_b^{ph} for CBO >0.4 eV, as evident in figure 5(a), which limits the flow of photogenerated electrons from the absorber to the buffer and thus photocurrent in the device. Consequently, a low FF in case of moderate barrier height and J_{SC} and V_{OC} in the case of high barrier height is observed.

It must be noted that although such a device with high φ_b^{ph}, as evident from figure 5(b), exhibits 'S shape' and consequently a very low FF, it does not exhibit rollover in the positive power quadrant, as observed in figure 2.

Next, let us look at the impact of scenario (ii) on the device *J–V* characteristics with no CBO at the CIGSu/buffer interface. The CIGSu device is simulated with different CBO at the buffer/i-layer interface, maintaining flat CBO at the CIGSu/buffer interface. The barrier φ_b^{in} was varied by varying the CBM of the

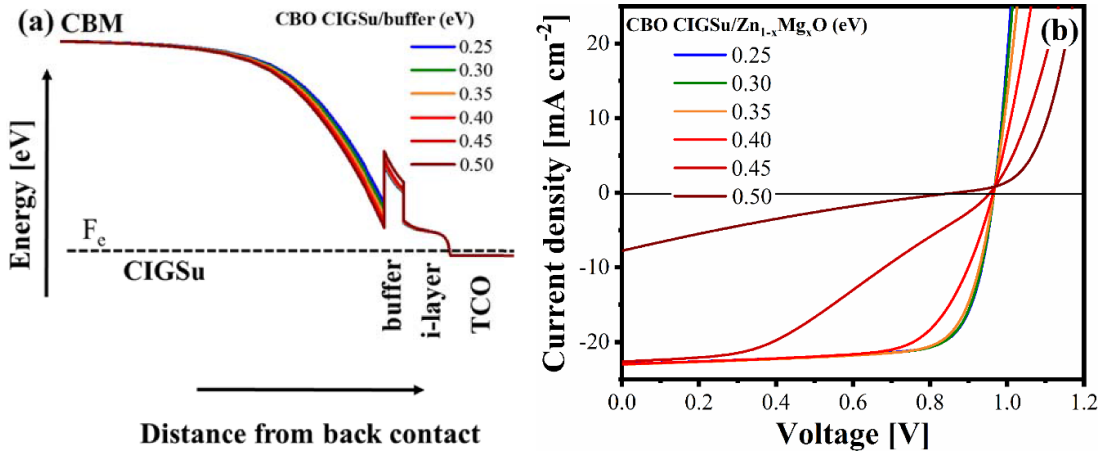

Figure 5. (a) Simulated band diagram and (b) *J–V* curves of CIGSu device with varying CBO at CIGSu/buffer interface maintaining a constant CBO (−0.2 eV) at buffer/i-layer interface and no CBO at the i-layer/TCO layer.

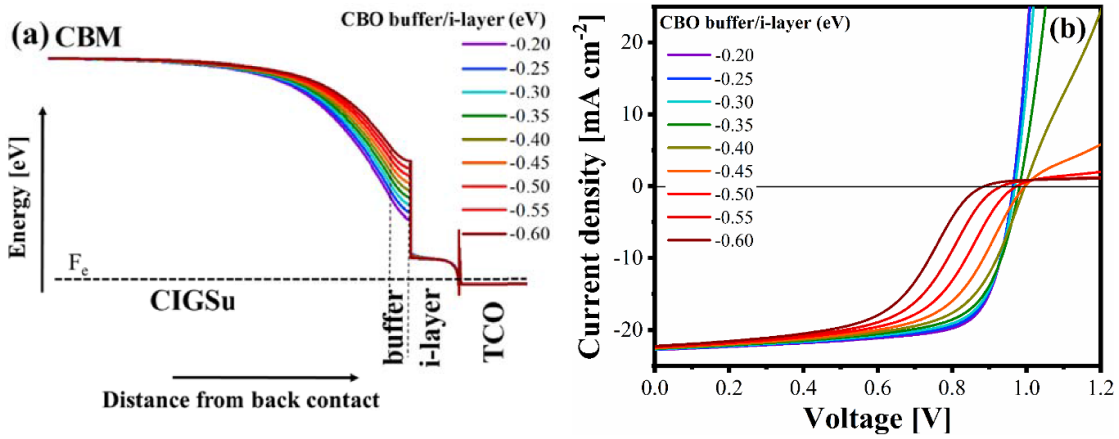

Figure 6. (a) Simulated band diagram and (b) *J–V* curves of CIGSu device with varying CBO at buffer/i-layer interface by changing the CBM of the i-layer and keeping the CBM of CIGSu and buffer layer at a fixed value to get a flat CBO at CIGSu/buffer interface.

i-layer and keeping the CBM of the buffer layer fixed at a value equal to the CBM of the absorber (i.e. with equal electron affinity). Such a device can be envisioned experimentally by varying Mg content in the (Zn,Mg)O i-layer without altering the Mg content in the $Zn_{1-x}Mg_xO$ buffer layer.

Figures 6(a) and (b) show the simulated band diagram and the *J–V* characteristics of such a device. The FF of the simulated devices deteriorates as the CBO at the buffer/i-layer interface decreases below −0.25 eV. Moreover, even the V_{OC} starts deteriorating for CBO values below <−0.50 eV. The drop in FF is a direct consequence of an 'S shape' in the form of a strong rollover in the positive power quadrant, which suggests blocking on injected carriers or conventional diode current in forward bias. The rollover is observed because the φ_b^{in} increases with increasing negative CBO at the buffer/i-layer interface (see figure 6(a)). Consequently, a higher potential drop is required in between the TCO and the buffer layer to drive the same amount of diode current through the device as for the lower negative CBO (as observed in figure 6(b)). The φ_b^{in} thus acts as a series resistance in the device and thus leads to a drop in FF. As the CBO or the φ_b^{in} at the buffer/i-layer increases, the series resistance also increases and the FF decreases.

It must be noted that when compared to the device with a high CBO at the absorber/buffer interface (i.e. case (i)), the drop in FF is not that substantial in these devices (see figure 6(b)). This fact is crucial, as it helps distinguish the effect of two barriers on the *J–V* properties of a device.

To understand the origin of V_{OC} reduction, the band diagrams of two exemplary devices are simulated at open-circuit conditions: one with a low negative CBO −0.2 eV and a high negative −0.6 eV CBO at the buffer/i-layer interface. Figures 7(a) and (b) show the respective simulated band diagrams. The drop in V_{OC} originates from the drop in electron Fermi level, as a drop in electron Fermi level near the buffer/i-layer interface is observed for the device with high negative CBO, something that is absent in the low negative

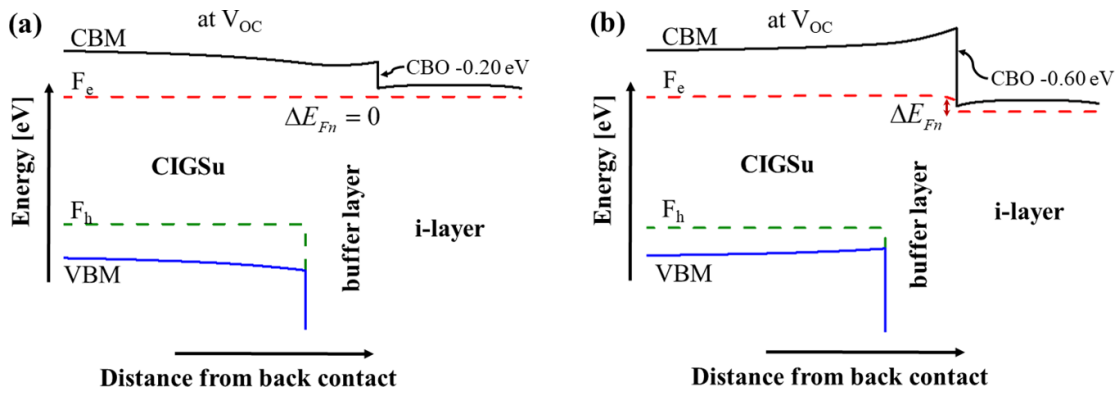

Figure 7. (a) and (b) show the simulated band diagram of the CIGSu device at open-circuit conditions with −0.20 and −0.60 eV CBO at the buffer/i-layer interface, respectively.

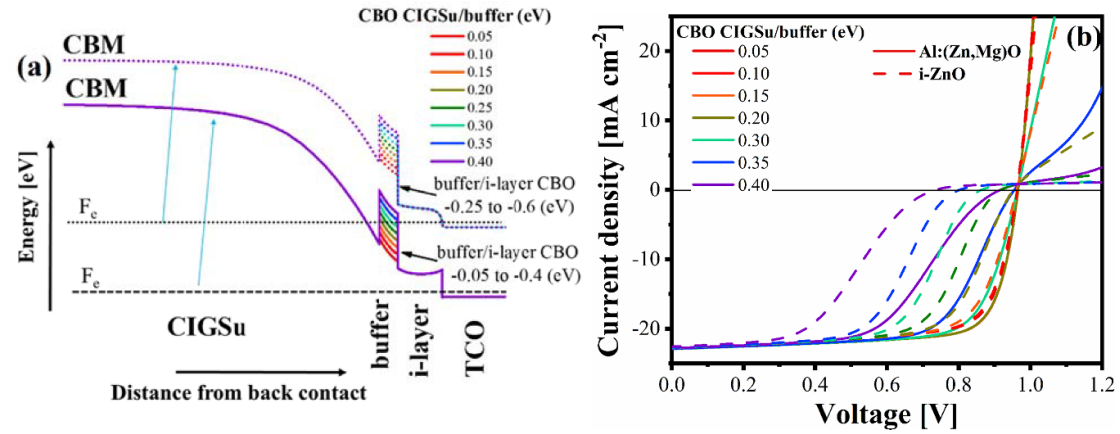

Figure 8. Simulated band diagram off-setted for clarity (a) and *J–V* curves of CIGSu device (b) with varying CBM position of buffer with either ZnO i-layer (dotted lines) or Al:(Zn,Mg)O i-layer (solid lines). With ZnO, the CBO at buffer/i-layer interface varies between −0.25 and −0.60 eV, whereas for Al:(Zn,Mg)O, it varies between −0.05 and −0.40 eV.

CBO device. This explains why the devices with ZnO i-layer have a higher interface V_{OC} deficit compared to Al:(Zn,Mg)O i-layer devices (table 1).

Finally, figures 8(a) and (b) show the simulated band diagram and the *J–V* characteristics of the CIGSu device with varying CBO at the CIGSu/buffer interface and buffer/i-layer interface. Experimentally, such a situation could be achieved by varying the Mg content in the $Zn_{1-x}Mg_xO$ buffer layer and keeping the Mg content fixed in the i-layer. Such a scenario most accurately fits the experimental part of this study. Assuming the increased bandgap in Al:(Zn,Mg)O i-layer is due to increased CBM energy, two device structures are simulated: one where the CBO at the CIGSu/buffer was varied from 0.05 to 0.40 eV, which consequently results in a −0.25 to −0.60 eV CBO at the buffer/i-layer, where i-layer is assumed to be Al:(Zn,Mg)O. Another, where the CBO at the CIGSu/buffer was also varied from 0.05 to 0.40 eV, but resulting in a −0.45 to −0.80 eV CBO at the buffer/i-layer, where i-layer is assumed to be ZnO. This was achieved by varying just the CBM of the buffer layer and keeping the CBM of the i-layer fixed at a value (4.4 and 4.6 eV, respectively, for Al:$Zn_{1-x}Mg_xO$ and ZnO i-layers).

The simulated *J–V* curves display 'S shape' in the negative power quadrant and rollover in the positive power quadrant as the CBM of buffer and consequently the CBO at the CIGSu/buffer interface increase beyond a specific value, which is different for both structures. For the Al:(Zn,Mg)O i-layer device, a significant distortion in the *J–V* curve is observable for CBO values above 0.35 eV, whereas for the ZnO i-layer device, the S shape and rollover are observable even for CBO values above 0.20 eV (see figure 8(b)). Consequently, in both cases, a drop in FF and V_{OC} is observed. Interestingly, for the same CBO value at the absorber/buffer interface, the drop in FF and V_{OC} is higher for ZnO i-layer simulated device. This is due to a higher negative CBO at the buffer/i-layer interface, as already discussed in case (ii). It is also in agreement with the experimental observation made in figure 2. Moreover, the drop in FF and V_{OC} increases as the CBM of the buffer increases in the simulations, similar to the observations made in figure 2, where increasing Mg

content in the (Zn,Mg)O buffer resulted in lower FF and V_{OC} independent of the i-layer. Therefore, the electrical barriers in the device can explain successfully the 'S shape' and rollover and, consequently, the loss in FF and V_{OC} observed in experiments.

To summarize, a high positive CBO at the absorber/buffer interface limits the photocurrent due to a high φ_b^{ph}, thus leading to 'S shape' in the negative power quadrant. A high negative CBO at the buffer/i-layer, on the other hand, reduces the diode current in the device due to a higher φ_b^{in}. Consequently, this leads to an increased series resistance in the device and in some cases to an 'S shape' in the positive power quadrant. In both scenarios, the FF of the device decreases due to electrical barriers.

5. Conclusions

Atomic layer-deposited (Zn,Mg)O and sputtered Al:(Zn,Mg)O were explored as a replacement for CdS buffer layer and ZnO i-layer in CIGSu solar cells with $E_G \sim 1.6$ eV. An optimum Mg concentration $x = 0.27$ in the $Zn_{1-x}Mg_xO$ buffer layer together with $x = 0.25$ Al:$Zn_{1-x}Mg_xO$ i-layer is found to deliver high device 14% PCE in the CIGSu device with bandgap ~1.6 eV.

Mg content above $x = 0.30$ in the $Zn_{1-x}Mg_xO$ buffer leads to an 'S shape' in the negative power quadrant because of photocurrent blocking due to a high CBO at the absorber/buffer interface. In addition, it leads to rollover in the positive power quadrant, which increases with the increasing Mg content in the $Zn_{1-x}Mg_xO$ buffer because the negative CBO at the $Zn_{1-x}Mg_xO$/i-layer interface increases. The Al:(Zn,Mg)O i-layer outperforms the traditional ZnO i-layer in terms of PCE, as it causes improvement in FF and the interface V_{OC} deficit. The gain is associated with a higher CBM and therefore lower CBO at the buffer/i-layer interface. Thus, we confirm Al:(Zn,Mg)O as a good substitute for traditional ZnO i-layer in CIGSu solar cells.

Numerical simulations show that a high CBO at the absorber/buffer interface alone leads to photocurrent blocking and therefore 'S shape' in the negative power quadrant. Also, a high CBO at the buffer/i-layer interface leads to diode current blocking and therefore a rollover in the positive power quadrant. When present together, they lead to 'S shape' in the negative power quadrant and rollover in the positive power quadrant and, consequently, reduce the FF of the device. In addition, a high negative CBO at the buffer/i-layer interface results in a drop in electron Fermi level at the interface, causing interface V_{OC} deficit in the devices.

In general, not only the CBO at the absorber/buffer but also the buffer/i-layer interface has a significant impact on solar cell characteristics. For the CIGSu device, the alternative buffer layers and i-layers must be chosen such that they have minimum CBO at the absorber/buffer and buffer/i-layer interface. Also, a low-temperature deposition process must be chosen for buffer and i-layer to preserve the qFLs and enhance the V_{OC} and, consequently, the PCE of the device.

Data availability statement

The data that support the findings of this study are available upon reasonable request from the authors.

Acknowledgments

This research was funded in whole, or in part, by the Luxembourg National Research Fund (Fonds National de la Recherche), Grant Reference [PRIDE 15/10935404/MASSENA] and [PRIDE17/12246511/PACE] project. For the purpose of open access, the author has applied a Creative Commons Attributions 4.0 International (CC BY 4.0) license to any Author Accepted Manuscript version arising from this submission.

We are grateful to Dr Marc Burgelman and his team at the University of Ghent, Belgium, for providing SCAPS-1D simulation software.

ORCID iDs

Mohit Sood https://orcid.org/0000-0002-2714-7737
Damilola Adeleye https://orcid.org/0000-0001-6359-9100
Renaud Leturcq https://orcid.org/0000-0001-7115-9172
Susanne Siebentritt https://orcid.org/0000-0001-6522-1427

References

[1] Jackson P, Hariskos D, Wuerz R, Kiowski O, Bauer A, Friedlmeier T M and Powalla M 2015 *Phys. Status Solidi* **9** 28
[2] Jackson P, Hariskos D, Lotter E, Paetel S, Wuerz R, Menner R, Wischmann W and Powalla M 2011 *Prog. Photovolt., Res. Appl.* **19** 894
[3] Jackson P, Wuerz R, Hariskos D, Lotter E, Witte W and Powalla M 2016 *Phys. Status Solidi* **10** 583

[4] Carron R, Nishiwaki S, Feurer T, Hertwig R, Avancini E, Löckinger J, Yang S C, Buecheler S and Tiwari A N 2019 *Adv. Energy Mater.* **9** 1900408
[5] Kato T, Wu J-L, Hirai Y, Sugimoto H and Bermudez V 2018 *IEEE J. Photovolt.* **9** 325
[6] Contreras M A, Ramanathan K, AbuShama J, Hasoon F, Young D L, Egaas B and Noufi R 2005 *Prog. Photovolt., Res. Appl.* **13** 209
[7] Weinhardt L, Heske C, Umbach E, Niesen T, Visbeck S and Karg F 2004 *Appl. Phys. Lett.* **84** 3175
[8] Rao G V, Säuberlich F and Klein A 2005 *Appl. Phys. Lett.* **87** 032101
[9] Tell B, Shay J L and Kasper H M 1971 *Phys. Rev.* B **4** 2463
[10] Weinhardt L, Fuchs O, Groß D, Storch G, Umbach E, Dhere N G, Kadam A A, Kulkarni S S and Heske C 2005 *Appl. Phys. Lett.* **86** 062109
[11] Morkel M, Weinhardt L, Lohmüller B, Heske C, Umbach E, Riedl W, Zweigart S and Karg F 2001 *Appl. Phys. Lett.* **79** 4482
[12] Shukla S, Sood M, Adeleye D, Peedle S, Kusch G, Dahliah D, Melchiorre M, Rignanese G-M, Hautier G and Oliver R 2021 *Joule* **5** 1816–31
[13] Minemoto T, Hashimoto Y, Satoh T, Negami T, Takakura H and Hamakawa Y 2001 *J. Appl. Phys.* **89** 8327
[14] Persson C, Platzer-Björkman C, Malmström J, Törndahl T and Edoff M 2006 *Phys. Rev. Lett.* **97** 146403
[15] Kieven D, Grimm A, Lauermann I, Lux-Steiner M C, Palm J, Niesen T and Klenk R 2012 *Phys. Status Solidi* **6** 294
[16] Khan I S, Muzzillo C P, Perkins C L, Norman A G, Young J L, Gaillard N and Zakutayev A 2021 *J. Phys. Energy* **3** 024001
[17] Hiroi H, Iwata Y, Adachi S, Sugimoto H and Yamada A 2016 *IEEE J. Photovolt.* **6** 760
[18] Hertwig R, Nishiwaki S, Ochoa M, Yang S-C, Feurer T, Gilshtein E, Tiwari A N and Carron R 2020 *EPJ Photovolt.* **11** 12
[19] Lee C-S, Shin Y M and Ahn B T 2011 *ECS Trans.* **41** 213
[20] Törndahl T, Platzer-Björkman C, Kessler J and Edoff M 2007 *Prog. Photovolt., Res. Appl.* **15** 225
[21] Kim S, Lee C-S, Kim S, Chalapathy R, Al-Ammar E A and Ahn B T 2015 *Phys. Chem. Chem. Phys.* **17** 19222
[22] Regesch D, Gütay L, Larsen J K, Deprédurand V, Tanaka D, Aida Y and Siebentritt S 2012 *Appl. Phys. Lett.* **101** 112108
[23] Babbe F, Choubrac L and Siebentritt S 2016 *Appl. Phys. Lett.* **109** 082105
[24] Inoue Y, Hála M, Steigert A, Klenk R and Siebentritt S 2015 Optimization of buffer layer/i-layer band alignment *2015 IEEE 42nd Photovoltaic Specialist Conf. (PVSC)* (IEEE) p 1
[25] Wurfel P 1982 *J. Phys. C: Solid State Phys.* **15** 3967
[26] Burgelman M, Nollet P and Degrave S 2000 *Thin Solid Films* **361–362** 527
[27] Scheer R and Schock H 2011 *Chalcogenide Photovoltaics* vol 9 (Hoboken, NJ: Wiley)
[28] Sood M, Urbaniak A, Kameni Boumenou C, Weiss T P, Elanzeery H, Babbe F, Werner F, Melchiorre M and Siebentritt S 2021 *Prog. Photovolt., Res. Appl.* **30** 263
[29] Scheer R 2009 *J. Appl. Phys.* **105** 104505
[30] Shockley W and Queisser H J 1961 *J. Appl. Phys.* **32** 510
[31] Niemegeers A and Burgelman M 1997 *J. Appl. Phys.* **81** 2881
[32] Scheer R and Schock H 2011 *Chalcogenide Photovoltaics* vol 305
[33] Niemegeers A, Gillis S and Burgelman M 1998 A user program for realistic simulation of polycrystalline heterojunction solar cells: SCAPS-1D *Proc. 2nd World Conf. on Photovoltaic Energy Conversion, JRC, European Commission* (*I-21020 Ispra (VA), Italy, July*) p 672